Host and viral determinants of airborne transmission of SARS-CoV-2 in the Syrian hamster

Julia R. Port*[1], Dylan H. Morris[2], Jade C. Riopelle[1], Claude Kwe Yinda[1], Victoria A. Avanzato[1], Myndi G. Holbrook[1], Trenton Bushmaker[1], Jonathan E. Schulz[1], Taylor A. Saturday[1], Kent Barbian[3], Colin A. Russell[4], Rose Perry-Gottschalk[5], Carl I. Shaia[6], Craig Martens[3], James O. Lloyd-Smith[2], Robert J. Fischer[1], Vincent J. Munster#[1]

1. *Laboratory of Virology, Division of Intramural Research, National Institute of Allergy and Infectious Diseases, National Institutes of Health, Hamilton, MT, USA*
2. *Department of Ecology and Evolutionary Biology, University of California, Los Angeles, CA, USA*
3. *Rocky Mountain Research and Technologies Branch, Division of Intramural Research, National Institute of Allergy and Infectious Diseases, National Institutes of Health, Hamilton, MT, USA*
4. *Department of Medical Microbiology | Amsterdam University Medical Center, University of Amsterdam*
5. *Rocky Mountain Visual and Medical Arts Unit, Research Technologies Branch, Division of Intramural Research, National Institute of Allergy and Infectious Diseases, National Institutes of Health, Hamilton, MT, USA*
6. *Rocky Mountain Veterinary Branch, Division of Intramural Research, National Institute of Allergy and Infectious Diseases, National Institutes of Health, Hamilton, MT, USA*

Corresponding author. vincent.munster@nih.gov

Author Contributions:

JRP designed the studies.

JRP, CKY, RJF, MGH, TB, KB performed the experiments, and DHM and JLS developed and analyzed the mathematical models.

JRP, VA, JCR, JES, CIS, KB, CM, KB, JLS, TAS analyzed results.

RPG generated figures.

JRP, DHM, JCR, JLS, VJM wrote the manuscript.

All co-authors reviewed the manuscript. This manuscript has been deposited as a preprint with bioRxiv under a CC0 license for government authors.

Competing Interest Statement: No competing interests to disclose.

Keywords: Transmission, SARS-CoV-2, Syrian hamster, aerosols

Summary

It remains poorly understood how SARS-CoV-2 infection influences the physiological host factors important for aerosol transmission. We assessed breathing pattern, exhaled droplets, and infectious virus after infection with Alpha and Delta variants of concern (VOC) in the Syrian hamster. Both VOCs displayed a confined window of detectable airborne virus (24-48 h), shorter than compared to oropharyngeal swabs. The loss of airborne shedding was linked to airway constriction resulting in a decrease of fine aerosols (1-10µm) produced, which are suspected to be the major driver of airborne transmission. Male sex was associated with increased viral replication and virus shedding in the air. Next, we compared the transmission efficiency of both variants and found no significant differences. Transmission efficiency varied mostly among donors, 0-100% (including a superspreading event), and aerosol transmission over multiple chain links was representative of natural heterogeneity of exposure dose and downstream viral kinetics. Co-infection with VOCs only occurred when both viruses were shed by the same donor during an increased exposure timeframe (24-48 h). This highlights that assessment of host and virus factors resulting in a differential exhaled particle profile is critical for understanding airborne transmission.

Main Text

Introduction

Transmission by aerosolized virus particles has been a major contributor to the spread of SARS-CoV-2 [1, 2] [3-6]. Although highly efficient in preventing severe disease, vaccines do not significantly reduce transmission of variants of concern (VOCs) [7]. Transmission occurs when people release respiratory droplets carrying virus during (e.g.) speaking, singing, breathing, sneezing, or coughing. Droplet size and half-life in the air are not uniform [8, 9] and depend on speech and breathing patterns [10], COVID-19 severity, and physiological parameters such as age [11, 12]. As with influenza [13], SARS-CoV-2 RNA was detectable mostly in fine aerosols in humans, as opposed to coarse aerosols [11]. It is not clear how exhaled droplet size, breathing patterns and even the quantity of exhaled infectious virus itself fundamentally contribute to the airborne transmission efficiency *in vivo* and how COVID-19 directly influences additional physiological factors which may contribute to fine aerosol production. There is reportedly large heterogeneity in the transmission potential of individuals. Superspreading events have been reported numerous times throughout the pandemic and are suggested to be a major driver [14, 15]. They are thought to arise from a combination of biological, social, and chance factors. While human epidemiology and modeling studies have highlighted various factors which may contribute to SARS-CoV-2 transmission heterogeneity, including viral load [16], much of the observed variance remains poorly understood. These factors are currently best studied in small animal models like the Syrian hamster, which allow for stringent and controlled experimental comparisons. The Syrian hamster model has been widely used to study SARS-CoV-2 transmission [17]; it recapitulates human contact, fomite and, importantly, airborne short distance and fine aerosol transmission [2, 18-20]. In this model, highest efficiency of short-distance airborne transmission was observed before onset of weight loss and acute lung pathology, peaking at one day post inoculation and correlating to the highest virus loads in the upper respiratory tract of donor animals [21]. Data on lung function loss in the Syrian hamster model after SARS-CoV-2 infection is available [22, 23], and virus has been demonstrated in exhaled droplets [24]. Yet, a systematic study that addresses how airborne transmission potential depends on these features, along with recognized influences of sex and VOC, has not been performed. The study of these contributing factors would allow us to address how they come together to shape transmission outcomes.

Here, we introduce a mathematical model delineating for Alpha and Delta VOCs the relationship between exhaled infectious virus and virus detected in the upper respiratory tract during infection and longitudinally

78 detail the changes in lung function, respiratory capacity, and exhaled particle profiles. Finally, we assess
79 the airborne transmission competitiveness and heterogeneity *in vivo* of Alpha and Delta.

80 **Results**

81 **Peak infectious SARS-CoV-2 in air samples is detected between 24 h and 48 h post infection**
82 Structural modelling and pseudotype-entry comparison suggested that the Syrian hamster model should
83 recapitulate the entry-specific competitive advantage of Delta over Alpha observed in humans (**Figure S**
84 **1A-D).** Syrian hamsters were inoculated with a low dose (10^3 $TCID_{50}$, intranasal (IN), N = 10 per group) of
85 SARS-CoV-2 Delta or Alpha. Animals were monitored for 14 days post inoculation (DPI). We observed no
86 significant differences in weight loss or viral titers in lung or nasal turbinates between the variants (**Figure**
87 **S 2A-C**). At 14 DPI, hamsters (N = 5) mounted a robust anti-spike IgG antibody response, and the overall
88 binding pattern was similar between Alpha and Delta (**Figure S 2D,E**). In a live virus neutralization assay,
89 homologous virus was neutralized significantly better as compared to the heterologous variant (**Figure S**
90 **2F,G**), but no significant difference was determined between the neutralization capacity against the
91 respective homologous variant (median reciprocal virus neutralization titer = 320 (Alpha anti-Alpha)/ 320
92 (Delta anti-Delta), p = 0.9568, N = 5, ordinary two-way ANOVA, followed by Tukey's multiple comparisons
93 test).
94 We determined the window of SARS-CoV-2 shedding for Alpha and Delta using swabs from the upper
95 respiratory tract and air sampling from cages, quantifying virus using gRNA, sgRNA, and infectious virus
96 titers. Oral swabs remained positive for gRNA and sgRNA until 7 DPI, but infectious virus dropped to
97 undetectable levels after 4 DPI in most individuals (**Figure S 3A)**. Cage air was sampled during the first 5
98 days of infection in 24 h time windows from cages containing 2 or 3 animals, grouped by sex. gRNA and
99 sgRNA were detectable as early as 1 DPI in 50% of air samples and remained high through 5 DPI, while
100 infectious virus peaked at on 2 DPI and was detectable for a shorter window, from 1 to 4 DPI (**Figure S**
101 **3B)**.
102
103 **Mathematical modeling demonstrates airborne shedding peaks later and declines faster than oral**
104 **swab viral load**
105 We quantified heterogeneity in shedding by variant, sex, and sampling method by fitting a mathematical
106 model of within-hamster virus kinetics (see **SI Mathematical Model**) to the data. This served to correlate
107 parameters which are easier to measure, such as RNA in the oral cavity, to the quantity of greatest interest
108 for understanding transmission (i.e. infectious virus in the air per unit time). To do this, we jointly inferred
109 the kinetics of shed airborne virus and parameters relating observable quantities (e.g., plaques from purified
110 air sample filters) to the actual longitudinal shedding. The inferential model uses mechanistic descriptions
111 of deposition of infectious virus into the air, uptake from the air, and loss of infectious virus in the

environment to extract estimates of the key parameters describing viral kinetics, as well as the resultant airborne shedding, for each animal. Virus was detectable and peaked earlier in oral swabs (approximately 24 h post inoculation) than virus sampled from the air (approximately 48 h post inoculation), and quantity of detected virus declined slower in the swabs (**Figure 1A,B**). gRNA and sgRNA declined slower than infectious virus both in the air and in swabs. Oral swab data was an imperfect proxy for airborne shedding, even when we directly quantified infectious virus titers. This was due to a lag between peak swab shedding and peak airborne shedding. Inferred within-host exponential growth and decay rates were similar for the two variants. For both variants, males shed more virus than females, even after accounting for males' higher respiration rates in measurements of shedding into the air. We found a slightly higher ratio of infectious virus to sgRNA in air samples for Delta than for Alpha (**Figure 1B, Figure S 3C,D).** We also found substantial individual-level heterogeneity in airborne shedding, even after accounting for sex and variant (**Figure 1B**). For example, air samples from cage 5 had more than twice as many peak plaques per capita than cage 6, even though both cages contained hamsters of the same sex, inoculated by the same dose, route, and variant. Our model captures this, with substantial inferred heterogeneity in individual airborne shedding in PFU per h, both in timing and in height of peak (**Figure 1B**)

Changes in breathing profile after SARS-CoV-2 infection precede onset of weight loss and are variant and sex-dependent

Pathology in nasal turbinates and lungs did not differ significantly between animals (**Figure S 4**). Pathological changes were consistent with those described previously for COVID-19 in Syrian hamsters after intranasal inoculation with other SARS-CoV-2 strains [19]. Whole body plethysmography (WBP) was performed. We focused the analysis on the first 5 days after inoculation, in which changes in virus shedding and release into the air were observed (**Figure S 2A**). Expiratory time (Te), inspiratory time (Ti), percentage of breath occupied by the transition from inspiration to expiration (TB), end expiratory pause (EEP), breathing frequency (f), peak inspiratory flow (PIFb), peak expiratory flow (PEFb), tidal volume (TVb), minute volume (MVb) and enhanced pause (Penh) were used to assess changes in pulmonary function throughout infection. Principal component analysis was used to determine trends in lung function changes across all groups (**Figure 2A**). This revealed a large degree of inherent variation in individual hamster plethysmography measures. Before inoculation there was no discernible pattern to the clustering observed besides a slight separation by sex. Beginning at 2 DPI, we observed a separation of infected and control animals. This coincided with the observation that all SARS-CoV-2 animals visibly decreased activity levels after 2 DPI, reducing exploratory activity and grooming with sporadic short convulsions which may represent coughing. No single parameter had an overwhelming influence on clustering, though several parameters contributed strongly across all days: Te, Ti, TB, EEP, f, PIFb, PEFb, TVb, and MVb (**Figure 2B,C**).

Broad patterns emerged by variant and by sex. Cumulative Penh AUC values for all infected groups were increased compared to the sex-matched control hamsters ($p = 0.022$, Kruskal-Wallis test, $N = 4$ for Alpha

147 and Delta, N = 5 for controls). The median Penh AUC values for Alpha, Delta, and control males were
148 0.741, 2.666, and 0.163, respectively (p = 0.062). The median Penh AUC values for Alpha females, Delta
149 females, and control females were 1.783, 2.255, and 0.159, respectively (p = 0.019). At 4 DPI, the median
150 fold change Penh values for Alpha males and Delta males were 0.793 and 1.929, respectively, as compared
151 to 0.857 for control males. The corresponding Penh values for Alpha, Delta, and control females were
152 1.736, 1.410, and 1.008, respectively. The separation on 4 DPI did not translate to significant changes in
153 more traditional measures of respiratory function, including f, TVb, and MVb.

154 **Changes in exhaled aerosol aerodynamic profile after SARS-CoV-2 infection precede acute disease,**
155 **are variant and sex-dependent**

156 Alpha and Delta inoculated groups (N = 10 each) and a control group (N = 10) were individually evaluated
157 on 0, 1, 3, and 5 DPI. To normalize the particle counts between animals we focused on the percentage of
158 particles in each size range. Across each variant group, particle diameter size <0.53 μm was the most
159 abundant (**Figure 3A**). No consistent, significant overall change in the number of overall particles across
160 all sizes was observed between groups (**Figure S 5C**). Particles between 1 and 10 μm in diameter, most
161 relevant for fine aerosol transmission [25], were examined. At baseline (0 DPI), females across all groups
162 produced a higher proportion of droplets in the 1-10 μm diameter range compared to males (**Figure 3A**).
163 At 3 DPI, the particle profiles shifted towards smaller aerodynamic diameters in the infected groups. At 5
164 DPI, even control animals demonstrated reduced exploratory behavior, resulting in a reduction of particles
165 in the 1-10 μm range, which could be due to acclimatization to the chamber. This resulted in an overall shift
166 in particle size from the 1-10 μm range to the <0.53 μm range. To analyze these data, individual slopes for
167 each animal were calculated using simple linear regression across the four timepoints (Percent ~ Intercept
168 + Slope $*$ Day) for percent of particles in the <0.53 μm range and percent of particles in the 1-10 μm range
169 and multiple linear regression was performed (**Figure 3B**). Females had a steeper decline at an average
170 rate of 2.2 per day after inoculation in the percent of 1-10 μm particles (and a steeper incline for <0.53 μm)
171 when compared to males, while holding variant group constant. When we compared variant group while
172 holding sex constant, we found that the Delta group had a steeper decline at an average rate of 5.6 per day
173 in the percent of 1-10 μm particles (and a steeper incline for <0.53 μm); a similar trend, but not as steep,
174 was observed for the Alpha group.

175 The estimated difference in slopes for Delta vs. controls and Alpha vs. controls in the percent of <0.53 μm
176 particles was 5.4 (two-sided adjusted p= 0.0001) and 2.4 (two-sided adjusted p = 0.0874), respectively.
177 The estimated difference in slopes for percent of 1-10 μm particles was not as pronounced, but similar
178 trends were observed for Delta and Alpha. Additionally, a linear mixed model was considered and produced

179 virtually the same results as the simpler analysis described above; the corresponding linear mixed model
180 estimates were the same and standard errors were similar.
181
182 **Alpha and Delta VOC attack rates reveal minimal individual risk of dual infection *in-vivo***
183 We next compared attack rates between Alpha and Delta during a 4 h exposure window at 200 cm distance.
184 Groups of sentinels (N = 4 or 5) were exposed to two donor animals, one inoculated with Alpha and one
185 inoculated with Delta **(Figure 4A**).
186 sgRNA in oral swabs taken on 1 DPI varied between animals (**Figure 4B**). Sentinels were either exposed
187 first for 2 h to one variant and then for 2 h to the second (**Figure 4C,** first 4 iterations), or to both variants
188 at the same time for 4 h (last three iterations). Transmission was confirmed by sgRNA in oral swabs
189 collected from all sentinels at 2, 3, and 5 DPE. On 2 DPE, N = 13/34 sentinels were positive for sgRNA in
190 oral swabs, N = 19/34 on 3 DPE and N = 27/34 on 5 DPE. Swabs from 3 DPE and 5 DPE were sequenced,
191 and the percentage of reads mapped to Alpha, and Delta were compared (**Figure 4D**).
192 All animals had only one variant detectable on day 3. In total, 12 sentinels were infected with Alpha and 7
193 with Delta by 3 DPE. At 5 DPE, slightly more sentinels shed Alpha (cartoon hamster representation in
194 Figure 4D depicts majority variant for each individual across both sampling days; **Table S 1** lists sequencing
195 results). Interestingly, we observed one superspreading event in iteration A, in which one donor animal
196 transmitted Alpha to all sentinels. For all other iterations, either both donors managed to transmit to at least
197 one sentinel, or not all sentinels were infected. For the iterations with simultaneous exposure, attack rates
198 were similar and statistically indistinguishable: Alpha = 50 %, Delta = 42.8 %. In one simultaneous exposure
199 (iteration F), three sentinels had both Delta and Alpha detectable at 5 DPE. In two, Delta was dominant,
200 and in one Alpha, always with the other variant in the clear minority (<15%). We did not observe any other
201 such coinfections (defined as a PCR positive animal with both Alpha and Delta at 5 % frequency or higher
202 by NGS). This led us to ask whether there was virus interference in sequential exposures - that is, whether
203 established infection with one variant could reduce the probability of successful infection given a later
204 exposure.
205 To assess this, we used our within-host dynamics model to calculate the estimated infection probabilities
206 for Alpha and Delta for each sentinel in each iteration, assuming each sentinel is exposed independently,
207 but accounting for the different exposure durations, donor sexes, and donor viral load (as measured by oral
208 swabs). From those probabilities, we then calculated posterior probability distributions for the number of
209 co-infections predicted to occur in each iteration if Alpha and Delta infections occurred independently and
210 did not interfere with each other (**Appendix Mathematical Model Figures M2-M4**). We found that our
211 observed coinfections were consistent with this null model; our data do not provide clear evidence of virus
212 interference during sequential exposure, though they also do not rule out such an effect. No difference in

213 virus replication or disease severity was observed between the sentinels infected with Alpha or Delta
214 (**Figure S 6**)
215

216 **Limited sustainability of heterologous VOC populations through multiple rounds of airborne**
217 **transmission**

218 To assess the transmission efficiency in direct competition between the Alpha and Delta VOCs, we
219 conducted an airborne transmission experiment over three subsequent rounds of exposure (**Figure 5A**).
220 Donor animals (N = 8) were inoculated IN with 5 x 10^2 $TCID_{50}$ of Alpha and 5 x 10^2 $TCID_{50}$ Delta (1:1 mixture)
221 and eight sentinels were exposed (Sentinels 1, 1:1 ratio) on 1 DPI for 24 h (first chain link, exposure window:
222 24-48 h post inoculation of the donors) (**Figure 5**). Two days after the start of this exposure, the eight
223 sentinels were placed into the donor side of a new cage and eight new sentinels (Sentinels 2) were exposed
224 for 24 h (second chain link, exposure window 48-72 h post exposure start of the Sentinels 1). Again, 2 days
225 after exposure start, this sequence was repeated for Sentinels 3 (third chain link, exposure window 48-72
226 h post exposure start of the Sentinels 2). All animals were individually housed between exposures, and
227 after exposure as well for the sentinels. We assessed viral presence in oropharyngeal swabs taken from
228 all animals at 2 and 5 DPI/DPE. While all Sentinels 1 demonstrated active shedding at 2 and 5 DPE, in the
229 Sentinels 2 group no viral RNA was detected in 2/8 animals and no infectious virus in 4/8 by 5 DPE. In the
230 Sentinels 3 group, sgRNA and infectious virus were only detected robustly in one animal on 5 DPE. In
231 contrast to donor animals, all infected sentinels exhibited higher shedding on day 5 compared to day 2 (2
232 DPI / 5 DPI Donors: median gRNA = 7.8 / 6.9 copies/mL (Log^{10}), median sgRNA = 7.2 / 6.4 copies/mL
233 (Log_{10})), median infectious virus titer = 2.3 / 0.5 $TCID_{50}$/mL (Log_{10}); Sentinels 1 (median gRNA = 7.2 / 7.4
234 copies/mL (Log_{10}), median sgRNA = 6.4 / 6.9 copies/mL (Log_{10}), median infectious virus titer = 2.9 / 2.6
235 $TCID_{50}$/mL (Log_{10}); Sentinels 2 = median gRNA = 3.7 / 5.4 copies/mL (Log_{10}), median sgRNA = 1.8 / 3.0
236 copies/mL (Log_{10}), median infectious virus titer = 0.5 / 1.6 $TCID_{50}$/mL (Log_{10})) (**Figure 5B**). Taken together,
237 this evidence suggests that the infectious shedding profile shifts later and decreases in magnitude with
238 successive generations of transmission. This could be explained by lower exposure doses causing lower
239 and slower infections in the recipients.
240 We then proceeded to compare the viral loads in the lungs and nasal turbinates at 5 DPE. Viral gRNA was
241 detected in the lungs (**Figure 5C**) and nasal turbinates (**Figure 5D**) of all Donors (lungs: median gRNA =
242 9.7 copies/gr tissue (Log_{10}), nasal turbinates: median gRNA = 6.2 copies/gr tissue (Log_{10})). Interestingly,
243 while the gRNA amount was similar in lungs between Donors and Sentinels 1 (lungs: median gRNA = 9.5
244 copies/gr tissue (Log_{10})), it was increased in nasal turbinates for the Sentinel 1 group (nasal turbinates:
245 median gRNA = 8.6 copies/gr tissue (Log_{10})). Similarly, sgRNA was increased in Sentinels 1 as compared
246 to Donors in nasal turbinates, but not lungs (Donors = lungs: median sgRNA = 9.4 copies/gr tissue (Log_{10}),
247 nasal turbinates: median sgRNA = 5.7 copies/gr tissue (Log10); Sentinels 1 = lungs: median sgRNA = 9.2

248 copies/gr tissue (Log_{10}), nasal turbinates: median sgRNA = 8.4 copies/gr tissue (Log_{10})). Viral gRNA above
249 the level of quantification was detectable in 6/8 Sentinels 2 in both lungs and nasal turbinates, yet sgRNA
250 was only detected in 4/8 Sentinels 2 in lungs and 5/8 in nasal turbinates. Even though gRNA was detected
251 in 3/8 Sentinels 3, no animal had detectable sgRNA in either lungs or nasal turbinates, signaling a lack of
252 active virus replication. To confirm this, infectious virus was analyzed in both tissues for the Donors,
253 Sentinels 1, and Sentinels 2 groups (**Figure 5E**). In both tissues titers were marginally higher in Sentinels
254 1 (median $TCID_{50}$ / gr tissue (Log_{10}) Donors: lungs = 8.6, nasal turbinates = 8.0; Sentinels 1: lungs = 8.9,
255 nasal turbinates = 8.8). Infectious virus was present in 6/8 Sentinels 2 in lungs and 5/8 in nasal turbinates.
256 Hence, even though the exposure interval for the second and third chain links were started 48 h after the
257 start of their own exposure, not all Sentinels 2 became infected, and only one Sentinel 3 animal became
258 infected and demonstrated shedding. We conducted a separate experiment to assess viral loads in the
259 respiratory tract after SARS-CoV-2 airborne transmission at 2 DPI/DPE. While infectious virus was present
260 in oral swabs from all sentinels, virus in lungs and nasal turbinates was not present in all animals (**Figure**
261 **S 7**).
262 To determine the competitiveness of the variants, we analyzed the relative composition of the two viruses
263 using next generation sequencing (**Figure 5F,G**). Neither variant significantly outcompeted the other. We
264 first compared the percentage of Delta in oral swabs taken on 2 DPI/DPE, the day of exposure of the next
265 chain link. In Donors, no variant was more prevalent across animals or clearly outcompeted the other within
266 one host (median = 56.5% Delta, range = 40.3-69%). After the first transmission event, Delta outcompeted
267 Alpha at 2 DPE (median = 87.3% Delta, range = 19-92.7%), while after the second transmission event, half
268 (N = 2/4) the animals shed either > 80% either Alpha or Delta. Notably, and in strong contrast to the dual
269 donor experiments described above, every sentinel animal exhibited a mixed infection at 2 DPE, often with
270 proportions resembling those in the donor.
271 Next, we looked at the selective pressure within the host. By 5 DPI/DPE, no clear difference was observed
272 in Donors (median = 60% Delta, range = 34.3-67.7%), but in the Sentinels 1 group Alpha overtook Delta in
273 three animals (median = 68.3% Delta, range = 17-92.3%), while the reverse was never seen. In one animal,
274 we observed a balanced infection established between both variants at 5 DPE (Sentinel 1.8). In the
275 Sentinels 2 group, Alpha was the dominant variant in N = 3/8 animals, and Delta dominated in 3/8 (median
276 = 55% Delta, range = 17-92.7%). The one Sentinel 3 animal for which transmission occurred shed nearly
277 exclusively Alpha. This suggests that within one host, Alpha was marginally more successful at
278 outcompeting Delta in the oropharyngeal cavity.
279 We then assessed virus sequences in lungs and nasal turbinates to understand if the selective pressure is
280 influenced by spatial dynamics. In Donor lungs, the percentage of Alpha was marginally higher on 5 DPI
281 (median = 42.3% Delta, range = 23.3-75.7%). In the Sentinels groups, either Alpha or Delta outcompeted
282 the other variant within each animal, only one animal (Sentinel 1.8) revealing both variants > 15%. In N =

283 5/8 Sentinels 1, yet only in N = 1/4 Sentinel 2 animals, Delta outcompeted Alpha. Sequencing of virus
284 isolated from nasal turbinates reproduced this pattern. In Donors, neither variant demonstrated a completive
285 advantage (median = 51.2% Delta, range = 38.7-89.3%). In N = 5/8 Sentinels 1, and N = 3/8 Sentinels 2,
286 Delta outcompeted Alpha. Combined a trend, while not significant, was observed for increased replication
287 of Delta after the first transmission event, but not after the second, and in the oropharyngeal cavity (swabs)
288 as opposed to lungs (**Figure 5H**) (Donors compared to Sentinels 1: $p = 0.0559$; Donors compared to
289 Sentinels 2: $p = >0.9999$; Kruskal Wallis test, followed by Dunn's test). Swabs taken at 2 DPI/DPE did
290 significantly predict variant patterns in swabs on 5 DPI/DPE (Spearman's $r = 0.623$, $p = 0.00436$) and virus
291 competition in the lower respiratory tract (Spearman's $r = 0.60$, $p = 0.00848$). Oral swab samples taken on
292 day 5 strongly correlate with both upper (Spearman's $r = 0.816$, $p = 0.00001$) and lower respiratory tract
293 tissue samples (Spearman's $r = 0.832$, $p = 0.00002$) taken on the same day (**Figure 5I**).
294
295 **Discussion**
296 In immunologically naïve humans, peak SARS-CoV-2 shedding occurs multiple days after exposure and in
297 some cases multiple days before onset of symptoms [26]. It is not known how this informs the window of
298 transmissibility, which is poorly understood and difficult to study in the absence of controlled exposures.
299 Measuring the quantity of exhaled virus and size distribution of airborne particles can provide additional
300 insight into the window of transmissibility beyond simply measuring infectious virus in upper respiratory tract
301 swabs. In addition, the shedding of virus in large and fine aerosols may be a function of physiological
302 changes after infection. Past studies in hamsters have shown that SARS-CoV-2 transmissibility is limited
303 to the first three days. This coincides with peak shedding and ends before the onset of weight loss, clinical
304 manifestation, and loss of infectious virus shedding in the upper respiratory tract [2, 18, 19]. We set out to
305 determine if SARS-CoV-2 infection affects host-derived determinants of airborne transmission efficiency
306 early after infection, which may explain this restriction.
307 Human studies have found similar peak viral RNA levels for Alpha and Delta [27, 28] despite their
308 epidemiological differences, including Delta's higher transmissibility [29], shorter generation interval [30],
309 and greater risk of severe disease [31]. We observe similar kinetics in a controlled experimental setting
310 using the hamster model. We found that swab viral load measurements are a valuable imperfect proxy for
311 the magnitude and timing of airborne shedding. Crucially, there is a period early in infection (around 24 h
312 post-infection in inoculated hamsters) when oral swabs show high infectious virus titers, but air samples
313 show low or undetectable levels of virus. Viral shedding should not be treated as a single quantity that rises
314 and falls synchronously throughout the host; spatial models of infection may be required to identify the best
315 correlates of airborne infectiousness [32]. Attempts to quantify an individual's airborne infectiousness from
316 swab measurements should thus be interpreted with caution, and these spatiotemporal factors should be
317 considered carefully.

318 While past studies have used whole body plethysmography to differentiate the impact of VOCs on lung
319 function, these have mostly focused on using mathematically derived parameters such as Penh, to compare
320 significant differences on pathology in late acute infection [23]. Within our experimental setup we observed
321 high variation within and between different hamsters. Observed differences could be contributed to the
322 behavioral state which correlated with sex, highlighting that future studies of this nature may require
323 increased acclimatization of the animals to these experimental procedures. However, we did observed
324 changes in breathing patterns as early as 2 DPI, preceding clinical symptoms, but coinciding with the
325 window of time when infectious virus was detected in the air.
326 The majority of SARS-CoV-2 exhaled from hamsters was observed within droplet nuclei <5 μm in size [27].
327 We report a rise in <0.53 μm particles and a drop in particles in the 1-10 μm range after infection. One of
328 the caveats of these measurements in small animals is that detected particles may come from aerosolized
329 fomites, and residual dust generated by movement [33]. In our system, we did not detect any particles
330 originating from dead animals or the environment, but we also saw a noticeable reduction of particles across
331 sizes when movement was minimal, or animals were deeply asleep. Considering the individual variability
332 in the lung function data, we did not observe that this shift in particle production was accompanied by a
333 consistent change in either breathing frequency, tidal volume, or minute volume. It remains to be
334 determined how well airway and particle size distribution dynamics in Syrian hamsters model those in
335 humans. Humans with COVID-19 have been shown to exhale fewer particles than uninfected individuals
336 during normal breathing, but not during coughing [34] and fine aerosols have been found to be the major
337 source of virus-loaded droplets. This suggests that a shorter duration of measurable infectious virus in air,
338 as opposed to the upper respiratory tract, could be partially due to early changes in airway constriction and
339 a reduction in exhaled particles of the optimal size range for transmission. The mechanisms involved in the
340 changing aerodynamic particle profile, and the distribution of viral RNA across particle sizes, require further
341 characterization in the hamster model.
342 Lastly, we compared the transmission efficiency of the Alpha and Delta variants in this system. We did not
343 find a clear transmission advantage for Delta over Alpha in Syrian hamsters, in either an attack rate
344 simulation or when comparing intra- and inter-host competitiveness over multiple generations of airborne
345 transmission. This contrasts sharply with epidemiological observations in the human population, where
346 Delta rapidly replaced Alpha (and other VOCs). The Syrian hamster model may not completely recapitulate
347 all aspects of SARS-CoV-2 virus kinetics and transmission in humans, particularly as the virus continues to
348 adapt to its human host.
349 Moreover, at the time of emergence of Delta, a large part of the human population was either previously
350 exposed to and/or vaccinated against SARS-CoV-2; that underlying host immune landscape also affects
351 the relative fitness of variants. Our naïve animal model does not capture the high prevalence of pre-existing
352 immunity preasent in the human population and may therefore be less relevant for studying overall variant

353 fitness in the current epidemiological context. Analyses of the cross-neutralization between Alpha and Delta
354 suggest subtly different antigenic profiles [35], and Delta's faster kinetics in humans may have also helped
355 it cause more reinfections and "breakthrough" infections [36].
356
357 Our two transmission experiments yielded different outcomes. When sentinel hamsters were sequentially
358 exposed, first to Alpha and then to Delta, generally no dual infections—both variants detectable—were
359 observed. In contrast, when we exposed hamsters simultaneously to one donor infected with Alpha and
360 another infected with Delta, we were able to detect mixed-variant virus populations in sentinels in one of
361 the cages (Cage F, Appendix Mathematical Model Figures M2, M3). The fact that we saw both single-
362 lineage and multi-lineage transmission events suggests that virus population bottlenecks at the point of
363 transmission do indeed depend on exposure mode and duration, as well as donor host shedding. Notably,
364 our analysis suggests that the Alpha-Delta co-infections observed in the Cage F sentinels could be due to
365 that being the one cage in which both the Alpha and the Delta donor shed substantially over the course of
366 the exposure (Appendix figures S2, S3). Mixed variant infections were not retained equally, and the relative
367 variant frequencies differed between investigated compartments of the respiratory tract, suggesting roles
368 for randomness or host-and-tissue specific differences in virus fitness.
369
370 A combination of host, environmental and virus parameters, many of which vary through time, play a role
371 in virus transmission. These include virus phenotype, shedding in air, individual variability and sex
372 differences, changes in breathing patterns, and droplet size distributions. Alongside recognized social and
373 environmental factors, these host and viral parameters might help explain why the epidemiology of SARS-
374 CoV-2 exhibits classic features of over-dispersed transmission [37]. Namely, SARS-CoV-2 circulates
375 continuously in the human population, but many transmission chains are self-limiting, while rarer
376 superspreading events account for a substantial fraction of the virus's total transmission. Heterogeneity in
377 the respiratory viral loads is high and some infected humans release tens to thousands of SARS-CoV-2
378 virions/min [38, 39]. Our findings recapitulate this in an animal model and provide further insights into
379 mechanisms underlying successful transmission events. Quantitative assessment of virus and host
380 parameters responsible for the size, duration and infectivity of exhaled aerosols may be critical to advance
381 our understanding of factors governing the efficiency and heterogeneity of transmission for SARS-CoV-2,
382 and potentially other respiratory viruses. In turn, these insights may lay the foundation for interventions
383 targeting individuals and settings with high risk of superspreading, to achieve efficient control of virus
384 transmission [40]."
385
386 **Materials and Methods**
387 *Ethics Statement*

388 All animal experiments were conducted in an AAALAC International-accredited facility and were approved
389 by the Rocky Mountain Laboratories Institutional Care and Use Committee following the guidelines put forth
390 in the Guide for the Care and Use of Laboratory Animals 8th edition, the Animal Welfare Act, United States
391 Department of Agriculture and the United States Public Health Service Policy on the Humane Care and
392 Use of Laboratory Animals. Protocol number 2021-034-E. Work with infectious SARS-CoV-2 virus strains
393 under BSL3 conditions was approved by the Institutional Biosafety Committee (IBC). For the removal of
394 specimens from high containment areas virus inactivation of all samples was performed according to IBC-
395 approved standard operating procedures.
396
397 *Cells and viruses*

398 SARS-CoV-2 variant Alpha (B.1.1.7) (hCoV320 19/England/204820464/2020, EPI_ISL_683466) was
399 obtained from Public Health England via BEI Resources. Variant Delta (B.1.617.2/) (hCoV-19/USA/KY-
400 CDC-2-4242084/2021, EPI_ISL_1823618) was obtained from BEI Resources. Virus propagation was
401 performed in VeroE6 cells in DMEM supplemented with 2% fetal bovine serum, 1 mM L-glutamine, 50 U/mL
402 penicillin and 50 µg/mL streptomycin (DMEM2). VeroE6 cells were maintained in DMEM supplemented
403 with 10% fetal bovine serum, 1 mM L- glutamine, 50 U/mL penicillin and 50 µg/ml streptomycin. No
404 mycoplasma and no contaminants were detected. All virus stocks were sequenced; no SNPs compared to
405 the patient sample sequence were detected in the Delta stock. In the Alpha stock we detected: ORF1AB
406 D3725G: 13% ORF1AB L3826F: 18%.
407
408 *Pseudotype entry assay*

409 The spike coding sequences for SARS-CoV-2 variant Alpha and Delta were truncated by deleting 19 aa at
410 the C-terminus. The S proteins with the 19 aa deletions of coronaviruses were previously reported to show
411 increased efficiency incorporating into virions of VSV [41, 42]. These sequences were codon optimized for
412 human cells, then appended with a 5′ kozak expression sequence (GCCACC) and 3′ tetra-glycine linker
413 followed by nucleotides encoding a FLAG-tag sequence (DYKDDDDK). These spike sequences were
414 synthesized and cloned into pcDNA3.1^{+}(GenScript). Human and hamster ACE2 (Q9BYF1.2 and
415 GQ262794.1, respectively) were synthesized and cloned into pcDNA3.1^{+} (GenScript). All DNA constructs
416 were verified by Sanger sequencing (ACGT). BHK cells were seeded in black 96-well plates and transfected
417 the next day with 100 ng plasmid DNA encoding human or hamster ACE2, using polyethylenimine
418 (Polysciences). All downstream experiments were performed 24 h post-transfection. Pseudotype
419 production was carried out as described previously [43]. Briefly, plates pre-coated with poly-L-lysine
420 (Sigma–Aldrich) were seeded with 293T cells and transfected the following day with 1,200 ng of empty
421 plasmid and 400 ng of plasmid encoding coronavirus spike or no-spike plasmid control (green fluorescent
422 protein (GFP)). After 24 h, transfected cells were infected with VSVΔG seed particles pseudotyped with

423 VSV-G as previously described [43, 44]. After one h of incubating with intermittent shaking at 37 °C, cells
424 were washed four times and incubated in 2 mL DMEM supplemented with 2% FBS, penicillin/streptomycin,
425 and L-glutamine for 48 h. Supernatants were collected, centrifuged at 500x*g* for 5 min, aliquoted, and stored
426 at −80 °C. BHK cells previously transfected with ACE2 plasmids of interest were inoculated with equivalent
427 volumes of pseudotype stocks. Plates were then centrifuged at 1200x*g* at 4 °C for 1 h and incubated
428 overnight at 37 °C. Approximately 18–20 h post-infection, Bright-Glo luciferase reagent (Promega) was
429 added to each well, 1:1, and luciferase was measured. Relative entry was calculated by normalizing the
430 relative light unit for spike pseudotypes to the plate relative light unit average for the no-spike control. Each
431 figure shows the data for two technical replicates.
432
433 *Structural interaction analysis*

434 The locations of the described spike mutations in the Alpha and Delta VOCs were highlighted on the SARS-
435 CoV-2 spike structure (PDB 6ZGE, [45]). To visualize the molecular interactions at the RBD-ACE2 binding
436 interface, the crystal structure of the Alpha variant RBD and human ACE2 complex (PDB 7EKF [46]) was
437 utilized. All figures were generated using The PyMOL Molecular Graphics System
438 (https://www.schrodinger.com/pymol).
439
440 *Aerosol caging*

441 Aerosol cages as described by Port *et al.* [2] were used for transmission experiments and air sampling as
442 indicated. The aerosol transmission system consisted of plastic hamster boxes (Lab Products) connected
443 by a plastic tube. The boxes were modified to accept a 7.62 cm (3') plastic sanitary fitting (McMaster-Carr),
444 which enabled the length between the boxes to be changed. Airflow was generated with a vacuum pump
445 (Vacuubrand) attached to the box housing the naïve animals and was controlled with a float-type
446 meter/valve (McMaster-Carr).
447
448 *Hamster infection with Alpha and Delta*

449 Four-to-six-week-old female and male Syrian hamsters (ENVIGO) were inoculated (10 animals per virus)
450 intranasally (IN) with either SARS-CoV-2 variant Alpha (B.1.1.7) (hCoV320 19/England/204820464/2020,
451 EPI_ISL_683466), variant Delta (B.1.617.2/) (hCoV-19/USA/KY-CDC-2-4242084/2021,
452 EPI_ISL_1823618)., or no virus (anesthesia controls). IN inoculation was performed with 40 µL sterile
453 DMEM containing 10^3 $TCID_{50}$ SARS-CoV-2 or simply sterile DMEM. At five days post inoculation (DPI), five
454 hamsters from each group were euthanized and tissues were collected. The remaining 5 animals were
455 euthanized at 14 DPI for disease course assessment and shedding analysis. For the control group, no day
456 5 necropsy was performed. Hamsters were weighed daily, and oropharyngeal swabs were taken on day 1,

457 2, 3, 4, 5, and 7. Swabs were collected in 1 mL DMEM with 200 U/mL penicillin and 200 µg/mL streptomycin.
458 For the control group, mock swabs were performed to ensure animals underwent the same anesthesia
459 protocols as infection groups. On day -1, 0, 1, 2, 3, 4, 5, 6, 7, and 14 whole body plethysmography was
460 performed. Profiles of particles produced by hamsters were collected on day 0, 1, 3, and 5. Cage air was
461 sampled on day 0, 1, 2, 3, 4, and 5. Hamsters were observed daily for clinical signs of disease. Necropsies
462 and tissue sampling were performed according to IBC-approved protocols.
463
464 *Air sampling of hamster cages*

465 During the first 5 days, hamsters were housed in modified aerosol cages (only one hamster box) hooked
466 up to an air pump. Air flow was generated at 30 cage changes/h. Between the cage and the pump a 47 mm
467 gelatin air filter was installed. Filters were exchanged in 24-h intervals. The filters were dissolved in 5 mL
468 of DMEM containing 10% FBS and presence of virus was determined by qRT PCR and plaque assay.
469
470 *Aerodynamic particle sizing of exhaled droplets*

471 Two strategies were used to measure the aerodynamic diameter of droplets exhaled by hamsters. SARS-
472 CoV-2 inoculated hamsters or uninfected control animals were placed into a 1.25 L isoflurane chamber.
473 This allowed free movement of the animal in the chamber. The chamber was hooked up with one port to a
474 HEPA filter. The second port was hooked up to a Model 3321 aerodynamic particle sizer spectrometer
475 (TSI). Both chamber and particle sizer were placed into a BSC class II cabinet. Animals remained in the
476 chamber for 5 x 1 min readings. For each set of readings, there were 52 different particle sizes. For each
477 hamster and timepoint, the total number of particles was calculated and the percent of particles in a
478 particular diameter range was derived using this total. RStudio 2021.09.1 Build 372 Ghost Orchid Release,
479 R version 4.1.2 (2021-11-01), Tidyverse R package version 1.3.1 (2021-04-15), and Emmeans R package
480 version 1.7.2 (2022-01-04) were used for the aerodynamic particle size analysis.
481 To differentiate between particle profiles produced by an awake and moving animal and those produced by
482 a sleeping animal with limited movement, uninfected age-matched hamsters (3 males and 2 female) were
483 acclimatized to being inside a 38.1 mm inside diameter tube hooked up to a particle sizer (**Figure S 5A,B**).
484 Both tube and particle sizer were placed into a BSC class II cabinet. To acclimate the animals to the tube,
485 sunflower seeds were provided to encourage investigation and free entry and exit from the tube. After
486 animals became used to being in the tube, ends were capped as depicted and 5 x 5 min readings were
487 taken. The particle size was measured using a Model 3321 aerodynamic particle sizer spectrometer (TSI).
488 Particle size profiles were analyzed using TSI software. As a control, particles originating from empty
489 enclosures and euthanized animals were recorded and found to be absent
490
491 *Aerosol transmission attack rate experiment*

492 Four-to-six-week-old female and male Syrian hamsters (ENVIGO) were used. In this experiment naïve
493 hamsters (sentinels) were exposed to donors infected with either Alpha or Delta in the same aerosol
494 transmission set-up to evaluate the attack rates of both variants. Donor hamsters were infected intranasally
495 as described above with 10^3 $TCID_{50}$ SARS-CoV-2 (Alpha or Delta, N = 7, respectively) and housed
496 individually. After 24 h, donor animals were placed into the donor cage. 4 or 5 sentinels were placed into
497 the sentinel cage (N = 34, 7 iterations), which was connected to the donor cage by a 2 m tube and exposed
498 for 4 h. Air flow was generated between the cages from the donor to the sentinel cage at 30 cage changes/h.
499 One donor inoculated with Alpha, and one donor inoculated with Delta were randomly chosen for each
500 scenario. Both donors were either placed together into the donor cage, or, alternatively, first one donor was
501 placed into the cage for 2 h, then the other for 2 h. To ensure no cross-contamination, the donor cages and
502 the sentinel cages were never opened at the same time, sentinel hamsters were not exposed to the same
503 handling equipment as donors, and equipment was disinfected with either 70% ETOH or 5% Microchem
504 after each sentinel. Regular bedding was replaced by alpha-dri bedding to avoid the generation of dust
505 particles. Oropharyngeal swabs were taken for donors after completion of the exposure and for sentinels
506 on days 2, 3, and 5 after exposure. Swabs were collected in 1 mL DMEM with 200 U/mL penicillin and 200
507 µg/mL streptomycin. Donors were euthanized after exposure ended, and sentinels were euthanized on day
508 5 for collection of lungs. All animals were always single housed outside the exposure window.
509
510 *Variant competitiveness transmission chain*

511 Four-to six-week-old female and male Syrian hamsters (ENVIGO) were used. Donor hamsters (N = 8) were
512 infected intranasally as described above with 10^3 $TCID_{50}$ SARS-CoV-2 at a 1:1 ratio of Alpha and Delta
513 (exact titration of the inoculum for both variants = 503 $TCID_{50}$, 80% Delta sequencing reads). After 12 h,
514 donor animals were placed into the donor cage and sentinels (Sentinels 1, N = 8) were placed into the
515 sentinel cage (1:1) at a 16.5 cm distance with an airflow of 30 cage changes/h as described by Port et al.
516 [2]. Hamsters were co-housed for 24 h. The following day, donor animals were re-housed into regular rodent
517 caging. One day later, Sentinels 1 were placed into the donor cage of new transmission set-ups. New
518 sentinels (Sentinels 2, N = 8) were placed into the sentinel cage at a 16.5 cm distance with an airflow of 30
519 changes/h. Hamsters were co-housed for 24 h. Then, Sentinels 1 were re-housed into regular rodent caging
520 and Sentinels 2 were placed into the donor cage of new transmission set-ups one day later. New sentinels
521 (Sentinels 3, N = 8) were placed into the sentinel cage at a 16.5 cm distance with an airflow of 30 changes/h.
522 Hamsters were co-housed for 24 h. Then both Sentinels 2 and Sentinels 3 were re-housed to regular rodent
523 caging and monitored until 5 DPE. Oropharyngeal swabs were taken for all animals at 2 and 5 DPI/DPE.
524 All animals were euthanized at 5 DPI/DPE for collection of lung tissue and nasal turbinates. To ensure no
525 cross-contamination, the donor cages and the sentinel cages were never opened at the same time, sentinel
526 hamsters were not exposed to the same handling equipment as donors, and the equipment was disinfected

527 with either 70% EtOH or 5% Microchem after each sentinel. Regular bedding was replaced by alpha-dri
528 bedding to avoid the generation of dust particles.
529
530 *Within-host kinetics model*

531 We used Bayesian inference to fit a semi-mechanistic model of within-host virus kinetics and shedding to
532 our data from inoculated hamsters. Briefly, the model assumes a period of exponential growth of virus within
533 the host up to a peak viral load, followed by exponential decay. It assumes virus shedding into the air follows
534 similar dynamics, and the time of peak air shedding and peak swab viral load may be offset from each other
535 by an inferred factor. Decay of RNA may be slower than that of infectious virus by an inferred factor,
536 representing the possibility, seen in our data, that some amplified RNA may be residual rather than
537 representative of current infectious virus levels. We also inferred conversion factors (ratios) among the
538 various quantities, i.e., how many oral swab sgRNA copies correspond to an infectious virion at peak viral
539 load. We fit the model to our swab and cage air sample data using Numpyro [47], which implements a No-
540 U-Turn Sampler [48]. For full mathematical details of the model and how it was fit, including prior distribution
541 choices and predictive checks (Appendix Mathematical Model Figure M1), see **Appendix: Within-host**
542 **dynamics model and Bayesian inference methods**.
543
544 *Whole body plethysmography*

545 Whole body plethysmography was performed on SARS-CoV-2 and uninfected Syrian hamsters. Animals
546 were individually acclimated to the plethysmography chamber (Buxco Electronics Ltd., NY, USA) for 20
547 minutes, followed by a 5-minute measurement period with measurements taken continuously and averaged
548 over two-second intervals. Initial data was found to have an especially high rejection index (Rinx) for
549 breaths, so was reanalyzed using a custom Buxco formula to account for differences between mice and
550 hamsters. This included expanding the acceptable balance range, the percent change in volume between
551 inhalation and exhalation, from 20-180% to 15-360%. Reanalysis using this algorithm resulted in the Rinx
552 across all hamsters from one day before infection to 5 days post-infection decreasing from 62.97% to
553 48.65%. The reanalyzed data were then used for further analysis. Each hamster's individual averages one
554 day prior to infection were used as their baselines for data analysis.
555 Areas under the curve (AUCs) for each parameter were calculated for each individual hamster based on
556 their raw deviation from baseline at each time point. Either positive or negative peaks were assessed based
557 on parameter-specific changes. Principal component analyses (PCAs) to visualize any potential clustering
558 of animals over the course of infection were performed for each day on raw values for each of the
559 parameters to accurately capture the true clustering with the least amount of data manipulation. PCAs and
560 associated visualizations were coded in R using RStudio version 1.4.1717 (RStudio Team, 2021). The
561 readxl package version 1.3.1 was then used to import Excel data into RStudio for analysis (Wickham and

562 Bryan, 2019). Only parameters that encapsulated measures of respiratory function were included (zero-
563 centered, scaled). The factoextra package version 1.0.1 (Kassambara and Mundt, 2020) was used to
564 determine the optimal number of clusters for each PCA via the average silhouette width method and results
565 were visualized using the ggplot2 package (Wickham, 2016). Correlation plots were generated based on
566 raw values for each lung function parameter using the corrplot package version 0.90 (Wei and Simko,
567 2021). The color palette for correlation plots was determined using RColorBrewer version 1.1-2 (Neuwirth,
568 2014).
569
570 *Viral RNA detection*

571 Swabs from hamsters were collected as described above. 140 µL was utilized for RNA extraction using the
572 QIAamp Viral RNA Kit (Qiagen) using QIAcube HT automated system (Qiagen) according to the
573 manufacturer's instructions with an elution volume of 150 µL. For tissues, RNA was isolated using the
574 RNeasy Mini kit (Qiagen) according to the manufacturer's instructions and eluted in 60 µL. Sub-genomic
575 (sg) and genomic (g) viral RNA were detected by qRT-PCR [49]. RNA was tested with TaqMan™ Fast Virus
576 One-Step Master Mix (Applied Biosystems) using QuantStudio 6 or 3 Flex Real-Time PCR System (Applied
577 Biosystems). SARS-CoV-2 standards with known copy numbers were used to construct a standard curve
578 and calculate copy numbers/mL or copy numbers/g. Limit of detection = 10 copies/rxn.
579
580 *Viral titration*

581 Viable virus in tissue samples was determined as previously described [15]. In brief, lung tissue samples
582 were weighed, then homogenized in 1 mL of DMEM (2% FBS). Swabs were used undiluted. VeroE6 cells
583 were inoculated with ten-fold serial dilutions of homogenate, incubated for 1 h at 37°C, and the first two
584 dilutions washed twice with 2% DMEM. For swab samples, cells were inoculated with ten-fold serial
585 dilutions and no wash was performed. After 6 days, cells were scored for cytopathic effect. $TCID_{50}$/mL was
586 calculated by the Spearman-Karber method. To determine titers in air samples, a plaque assay was used.
587 VeroE6 cells were inoculated with 200 µL/well (48-well plate) of undiluted samples, no wash was performed.
588 Plates were spun for 1 h at RT at 1000 rpm. 800 µL of CMC (500 mL MEM (Cat#10370, Gibco, must contain
589 NEAA), 5 mL PenStrep, 7.5 g carboxymethylcellulose (CMC, Cat# C4888, Sigma, sterilize in autoclave)
590 overlay medium was added to each well and plates incubated for 6-days at 37°C. Plates were fixed with
591 10% formalin overnight, then rinsed and stained with 1% crystal violet for 10 min. Plaques were counted.
592
593 *Serology*

594 Serum samples were analyzed as previously described [50]. In brief, maxisorp plates (Nunc) were coated
595 with 50 ng spike protein (generated in-house, purified recombinant) per well. Plates were incubated

596 overnight at 4°C. Plates were blocked with casein in phosphate buffered saline (PBS) (ThermoFisher) for
597 1 h at room temperature (RT). Serum was diluted 2-fold in blocking buffer and samples (duplicate) were
598 incubated for 1 h at RT. Secondary goat anti-hamster IgG Fc (horseradish peroxidase (HRP)-conjugated,
599 Abcam) spike-specific antibodies were used for detection and KPL TMB 2-component peroxidase substrate
600 kit (SeraCare, 5120-0047) was used for visualization. The reaction was stopped with KPL stop solution
601 (Seracare) and plates were read at 450 nm. The threshold for positivity was calculated as the average plus
602 3 x the standard deviation of negative control hamster sera.
603
604 *MesoPlex Assay*

605 The V-PLEX SARS-CoV-2 Panel 13 (IgG) kit from Meso Scale Discovery was used to test binding
606 antibodies against spike protein of SARS-CoV-2 with 10,000-fold diluted serum obtained from hamsters 14
607 DPI. A standard curve of pooled hamster sera positive for SARS-CoV-2 spike protein was serially diluted
608 4-fold. The secondary antibody was prepared by conjugating a goat anti-hamster IgG cross-adsorbed
609 secondary antibody (ThermoFisher) using the MSD GOLD SULFO-TAG NHS-Ester Conjugation Pack
610 (MSD). The secondary antibody was diluted 10,000X for use on the assay. The plates were prepped, and
611 samples were run according to the kit's instruction manual. After plates were read by the MSD instrument,
612 data was analyzed with the MSD Discovery Workbench Application.
613
614 *Virus neutralization*

615 Heat-inactivated γ-irradiated sera were two-fold serially diluted in DMEM. 100 $TCID_{50}$ of SARS-CoV-2
616 variant Alpha (B.1.1.7) (hCoV320 19/England/204820464/2020, EPI_ISL_683466) or variant Delta
617 (B.1.617.2/) (hCoV-19/USA/KY-CDC-2-4242084/2021, EPI_ISL_1823618) was added. After 1 h of
618 incubation at 37°C and 5% CO_2, the virus:serum mixture was added to VeroE6 cells. CPE was scored after
619 5 days at 37°C and 5% CO_2. The virus neutralization titer was expressed as the reciprocal value of the
620 highest dilution of the serum that still inhibited virus replication. The antigenic map was constructed as
621 previously described [51, 52] using the antigenic cartography software from https://acmacs-web.antigenic-
622 cartography.org. In brief, this approach to antigenic mapping uses multidimensional scaling to position
623 antigens (viruses) and sera in a map to represent their antigenic relationships. The maps here relied on the
624 first SARS-CoV-2 infection serology data of Syrian hamsters. The positions of antigens and sera were
625 optimized in the map to minimize the error between the target distances set by the observed pairwise virus-
626 serum combinations. Maps were effectively constructed in only one dimension because sera were only
627 titrated against two viruses and the dimensionality of the map is constrained to the number of test antigens
628 minus one.
629
630 *Next-generation sequencing of virus*

631 Total RNA was extracted from oral swabs, lungs, and nasal turbinates using the Qia Amp Viral kit (Qiagen,
632 Germantown, MD), eluted in EB, and viral Ct values were calculated using real-time PCR. Subsequently,
633 11 µL of extracted RNA was used as a template in the ARTIC nCoV-2019 sequencing protocol V.1
634 (Protocols.io - https://www.protocols.io/view/ncov-2019-sequencing-protocol-bbmuik6w) to generate 1st-
635 strand cDNA. Five microliters were used as template for Q5 HotStart Pol PCR (Thermo Fisher Sci,
636 Waltham, MA) together with 10 uM stock of a single primer pair from the ARTIC nCoV-2019 v3 Panel
637 (Integrated DNA Technologies, Belgium), specifically 76L_alt3 and 76R_alt0. Following 35 cycles and 55°C
638 annealing temperature, products were AmPure XP cleaned and quantitated with Qubit (Thermo Fisher Sci)
639 fluorometric quantitation per instructions. Following visual assessment of 1 µL on a Tape Station D1000
640 (Agilent Technologies, Santa Clara, CA), a total of 400 ng of product was taken directly into TruSeq DNA
641 PCR-Free Library Preparation Guide, Revision D (Illumina, San Diego, CA) beginning with the Repair Ends
642 step (q.s. to 60 µL with RSB). Subsequent cleanup consisted of a single 1:1 AmPure XP/reaction ratio and
643 all steps followed the manufacturer's instructions including the Illumina TruSeq CD (96) Indexes. Final
644 libraries were visualized on a BioAnalyzer HS chip (Agilent Technologies) and quantified using KAPA
645 Library Quant Kit - Illumina Universal qPCR Mix (Kapa Biosystems, Wilmington, MA) on a CFX96 Real-
646 Time System (BioRad, Hercules, CA). Libraries were diluted to 2 nM stock, pooled together in equimolar
647 concentrations, and sequenced on the Illumina MiSeq instrument (Illumina) as paired-end 2 X 250 base
648 pair reads. Because of the limited diversity of a single-amplicon library, 20% PhiX was added to the final
649 sequencing pool to aid in final sequence quality. Raw fastq reads were trimmed of Illumina adapter
650 sequences using cutadapt version 1.1227, then trimmed and filtered for quality using the FASTX-Toolkit
651 (Hannon Lab, CSHL). To process the ARTIC data, a custom pipeline was developed [53]. Fastq read pairs
652 were first compared to a database of ARTIC primer pairs to identify read pairs that had correct, matching
653 primers on each end. Once identified, the ARTIC primer sequence was trimmed off. Read pairs that did not
654 have the correct ARTIC primer pairs were discarded. Remaining read pairs were collapsed into one
655 sequence using AdapterRemoval [54] requiring a minimum 25 base overlap and 300 base minimum length,
656 generating ARTIC amplicon sequences. Identical amplicon sequences were removed, and the unique
657 amplicon sequences were then mapped to the SARS-CoV-2 genome (MN985325.1) using Bowtie2 [55].
658 Aligned SAM files were converted to BAM format, then sorted and indexed using SAMtools [56]. Variant
659 calling was performed using Genome Analysis Toolkit (GATK, version 4.1.2) HaplotypeCaller with ploidy
660 set to 2 [57]. Single nucleotide polymorphic variants were filtered for QUAL > 200 and quality by depth (QD)
661 > 20 and indels were filtered for QUAL > 500 and QD > 20 using the filter tool in bcftools, v1.9 [56]. Pie
662 charts were generated using ggplot2 (Wickham, 2016) in R 4.2.1 using RStudio version 1.4.1717 (RStudio
663 Team, 2021).
664
665 *Histopathology*

666 Necropsies and tissue sampling were performed according to IBC-approved protocols. Tissues were fixed
667 for a minimum of 7 days in 10% neutral buffered formalin with 2 changes. Tissues were placed in cassettes
668 and processed with a Sakura VIP-6 Tissue Tek on a 12-h automated schedule using a graded series of
669 ethanol, xylene, and ParaPlast Extra. Prior to staining, embedded tissues were sectioned at 5 µm and dried
670 overnight at 42°C. Using GenScript U864YFA140-4/CB2093 NP-1 (1:1000), specific anti-CoV
671 immunoreactivity was detected using the Vector Laboratories ImPress VR anti-rabbit IgG polymer (# MP-
672 6401) as secondary antibody. The tissues were then processed using the Discovery Ultra automated
673 processor (Ventana Medical Systems) with a ChromoMap DAB kit Roche Tissue Diagnostics (#760-159).
674
675 *Statistical Analysis*

676 Significance tests were performed as indicated where appropriate for the data using GraphPad Prism 9.
677 Unless stated otherwise, statistical significance levels were determined as follows: ns = $p > 0.05$; * = $p \leq$
678 0.05; ** = $p \leq 0.01$; *** = $p \leq 0.001$; **** = $p \leq 0.0001$. Exact nature of tests is stated where appropriate.
679
680 *Data availability statement*

681 Data deposited in Figshare (10.6084/m9.figshare.20493045) and Github (https://github.com/dylanhmorris/host-
682 viral-determinants).
683
684 **Acknowledgements**
685 We would like to thank Ryan Stehlik, Seth Cooley and Shanda Sarchette, and the animal care takers for
686 their assistance during the study. The following reagent was obtained through BEI Resources, NIAID, NIH:
687 SARS-CoV-2 variant Alpha (B.1.1.7) (hCoV320 19/England/204820464/2020, EPI_ISL_683466) and
688 variant Delta (B.1.617.2/) (hCoV-19/USA/KY-CDC-2-4242084/2021, EPI_ISL_1823618). We thank Neeltje
689 van Doremalen, Emmie de Wit, Brandi Williamson, Sujatha Rashid, Ranjan Mukul, Kimberly Stemple, Bin
690 Zhou, Natalie Thornburg, Sue Tong, Stacey Ricklefs, Sarah Anzick for gracefully sharing viruses or
691 propagating and sequencing stocks. We would like to thank Amy Tillman for assistance with the
692 aerodynamic particle data analysis.
693
694 **Funding**
695 This work was supported by the Intramural Research Program of the National Institute of Allergy and
696 Infectious Diseases (NIAID), National Institutes of Health (NIH) (1ZIAAI001179-01). JOL-S and DHM were
697 supported by the Defense Advanced Research Projects Agency DARPA PREEMPT (D18AC00031), the
698 UCLA AIDS Institute and Charity Treks, the 3Rs Pilot Studies program of the UCLA Animal Research
699 Committee, and the U.S. National Science Foundation (DEB-1557022). This work was part of NIAIDs
700 SARS-CoV-2 Assessment of Viral Evolution (SAVE) Program.

References

1. Zhang, R., et al., *Identifying airborne transmission as the dominant route for the spread of COVID-19.* Proc Natl Acad Sci U S A, 2020. **117**(26): p. 14857-14863.
2. Port, J.R., et al., *Increased small particle aerosol transmission of B.1.1.7 compared with SARS-CoV-2 lineage A in vivo.* Nature Microbiology, 2022. **7**(2): p. 213-223.
3. Boone, S.A. and C.P. Gerba, *Significance of Fomites in the Spread of Respiratory and Enteric Viral Disease.* Applied and Environmental Microbiology, 2007. **73**(6): p. 1687-1696.
4. Goldman, E., *Exaggerated risk of transmission of COVID-19 by fomites.* Lancet Infect Dis, 2020. **20**(8): p. 892-893.
5. CDC, *How COVID-19 Spreads.* 2021.
6. Pitol, A.K. and T.R. Julian, *Community Transmission of SARS-CoV-2 by Surfaces: Risks and Risk Reduction Strategies.* Environmental Science & Technology Letters, 2021. **8**(3): p. 263-269.
7. CDC. *SARS-CoV-2 Variant Classifications and Definitions*. 2021 [cited 2021 18 January 2022].
8. Morawska, L., et al., *Size distribution and sites of origin of droplets expelled from the human respiratory tract during expiratory activities.* Journal of Aerosol Science, 2009. **40**(3): p. 256-269.
9. Stadnytskyi, V., et al., *The airborne lifetime of small speech droplets and their potential importance in SARS-CoV-2 transmission.* Proceedings of the National Academy of Sciences, 2020. **117**(22): p. 11875-11877.
10. Johnson, G.R. and L. Morawska, *The mechanism of breath aerosol formation.* J Aerosol Med Pulm Drug Deliv, 2009. **22**(3): p. 229-37.
11. Coleman, K.K., et al., *Viral Load of Severe Acute Respiratory Syndrome Coronavirus 2 (SARS-CoV-2) in Respiratory Aerosols Emitted by Patients With Coronavirus Disease 2019 (COVID-19) While Breathing, Talking, and Singing.* Clinical Infectious Diseases, 2021.
12. Edwards, D.A., et al., *Exhaled aerosol increases with COVID-19 infection, age, and obesity.* Proceedings of the National Academy of Sciences, 2021. **118**(8): p. e2021830118.
13. Milton, D.K., et al., *Influenza Virus Aerosols in Human Exhaled Breath: Particle Size, Culturability, and Effect of Surgical Masks.* PLOS Pathogens, 2013. **9**(3): p. e1003205.
14. Sun, K., et al., *Transmission heterogeneities, kinetics, and controllability of SARS-CoV-2.* Science, 2021. **371**(6526): p. eabe2424.
15. Yang, Q., et al., *Just 2% of SARS-CoV-2−positive individuals carry 90% of the virus circulating in communities.* Proceedings of the National Academy of Sciences, 2021. **118**(21): p. e2104547118.
16. Goyal, A., et al., *Viral load and contact heterogeneity predict SARS-CoV-2 transmission and super-spreading events.* eLife, 2021. **10**: p. e63537.
17. Muñoz-Fontela, C., et al., *Animal models for COVID-19.* Nature, 2020. **586**(7830): p. 509-515.

744 18. Sia, S.F., et al., *Pathogenesis and transmission of SARS-CoV-2 in golden hamsters.*
745 Nature, 2020. **583**(7818): p. 834-838.
746 19. Rosenke, K., et al., *Defining the Syrian hamster as a highly susceptible preclinical model*
747 *for SARS-CoV-2 infection.* Emerg Microbes Infect, 2020. **9**(1): p. 2673-2684.
748 20. Port, J.R., et al., *SARS-CoV-2 disease severity and transmission efficiency is increased*
749 *for airborne compared to fomite exposure in Syrian hamsters.* Nat Commun, 2021. **12**(1):
750 p. 4985.
751 21. Ganti, K., et al., *Timing of exposure is critical in a highly sensitive model of SARS-CoV-2*
752 *transmission.* PLOS Pathogens, 2022. **18**(3): p. e1010181.
753 22. Port, J.R., et al., *High-Fat High-Sugar Diet-Induced Changes in the Lipid Metabolism*
754 *Are Associated with Mildly Increased COVID-19 Severity and Delayed Recovery in the*
755 *Syrian Hamster.* Viruses, 2021. **13**(12): p. 2506.
756 23. Halfmann, P.J., et al., *SARS-CoV-2 Omicron virus causes attenuated disease in mice and*
757 *hamsters.* Nature, 2022. **603**(7902): p. 687-692.
758 24. Hawks, S.A., et al., *Infectious SARS-CoV-2 Is Emitted in Aerosol Particles.* mBio, 2021.
759 **12**(5): p. e0252721-e0252721.
760 25. Wang, C.C., et al., *Airborne transmission of respiratory viruses.* Science, 2021.
761 **373**(6558): p. eabd9149.
762 26. Jones, T.C., et al., *Estimating infectiousness throughout SARS-CoV-2 infection course.*
763 Science, 2021. **373**(6551): p. eabi5273.
764 27. Kissler, S.M., et al., *Viral Dynamics of SARS-CoV-2 Variants in Vaccinated and*
765 *Unvaccinated Persons.* New England Journal of Medicine, 2021. **385**(26): p. 2489-2491.
766 28. Elie, B., et al., *Variant-specific SARS-CoV-2 within-host kinetics.* J Med Virol, 2022.
767 29. Earnest, R., et al., *Comparative transmissibility of SARS-CoV-2 variants Delta and Alpha*
768 *in New England, USA.* Cell Reports Medicine, 2022. **3**(4): p. 100583.
769 30. Hart, W.S., et al., *Generation time of the alpha and delta SARS-CoV-2 variants: an*
770 *epidemiological analysis.* The Lancet Infectious Diseases, 2022. **22**(5): p. 603-610.
771 31. Twohig, K.A., et al., *Hospital admission and emergency care attendance risk for SARS-*
772 *CoV-2 delta (B.1.617.2) compared with alpha (B.1.1.7) variants of concern: a cohort*
773 *study.* The Lancet Infectious Diseases, 2022. **22**(1): p. 35-42.
774 32. Snedden, C.E., et al., *SARS-CoV-2: Cross-scale Insights from Ecology and Evolution.*
775 Trends in Microbiology, 2021. **29**(7): p. 593-605.
776 33. Asadi, S., et al., *Non-respiratory particles emitted by guinea pigs in airborne disease*
777 *transmission experiments.* Scientific Reports, 2021. **11**(1): p. 17490.
778 34. Viklund, E., et al., *Severe acute respiratory syndrome coronavirus 2 can be detected in*
779 *exhaled aerosol sampled during a few minutes of breathing or coughing.* Influenza and
780 Other Respiratory Viruses, 2022. **16**(3): p. 402-410.
781 35. van Doremalen, N., et al., *ChAdOx1 nCoV-19 (AZD1222) or nCoV-19-Beta (AZD2816)*
782 *protect Syrian hamsters against Beta Delta and Omicron variants.* Nat Commun, 2022.
783 **13**(1): p. 4610.
784 36. Yang, W. and J. Shaman, *Viral replication dynamics could critically modulate vaccine*
785 *effectiveness and should be accounted for when assessing new SARS-CoV-2 variants.*
786 Influenza Other Respir Viruses, 2022. **16**(2): p. 366-367.

37. Lloyd-Smith, J.O., et al., *Superspreading and the effect of individual variation on disease emergence.* Nature, 2005. **438**(7066): p. 355-359.
38. Chen, P.Z., et al., *Heterogeneity in transmissibility and shedding SARS-CoV-2 via droplets and aerosols.* Elife, 2021. **10**.
39. Majra, D., et al., *SARS-CoV-2 (COVID-19) superspreader events.* J Infect, 2021. **82**(1): p. 36-40.
40. Kain, M.P., et al., *Chopping the tail: how preventing superspreading can help to maintain COVID-19 control.* medRxiv, 2020.
41. Fukushi, S., et al., *Vesicular stomatitis virus pseudotyped with severe acute respiratory syndrome coronavirus spike protein.* Journal of General Virology, 2005. **86**(8): p. 2269-2274.
42. Kawase, M., et al., *Protease-Mediated Entry via the Endosome of Human Coronavirus 229E.* Journal of Virology, 2009. **83**(2): p. 712-721.
43. Letko, M., A. Marzi, and V. Munster, *Functional assessment of cell entry and receptor usage for SARS-CoV-2 and other lineage B betacoronaviruses.* Nature Microbiology, 2020. **5**(4): p. 562-569.
44. Takada, A., et al., *A system for functional analysis of Ebola virus glycoprotein.* Proceedings of the National Academy of Sciences, 1997. **94**(26): p. 14764-14769.
45. Wrobel, A.G., et al., *SARS-CoV-2 and bat RaTG13 spike glycoprotein structures inform on virus evolution and furin-cleavage effects.* Nature Structural & Molecular Biology, 2020. **27**(8): p. 763-767.
46. Han, P., et al., *Molecular insights into receptor binding of recent emerging SARS-CoV-2 variants.* Nature Communications, 2021. **12**(1): p. 6103.
47. Phan, D., N. Pradhan, and M. Jankowiak, *Composable effects for flexible and accelerated probabilistic programming in NumPyro.* arXiv preprint arXiv:1912.11554, 2019.
48. Hoffman, M.D. and A. Gelman, *The No-U-Turn sampler: adaptively setting path lengths in Hamiltonian Monte Carlo.* J. Mach. Learn. Res., 2014. **15**(1): p. 1593-1623.
49. Corman, V.M., et al., *Detection of 2019 novel coronavirus (2019-nCoV) by real-time RT-PCR.* Euro Surveill, 2020. **25**(3).
50. Yinda, C.K., et al., *K18-hACE2 mice develop respiratory disease resembling severe COVID-19.* PLoS Pathog, 2021. **17**(1): p. e1009195.
51. Smith, D.J., et al., *Mapping the Antigenic and Genetic Evolution of Influenza Virus.* Science, 2004. **305**(5682): p. 371-376.
52. Fonville, J.M., et al., *Antibody landscapes after influenza virus infection or vaccination.* Science, 2014. **346**(6212): p. 996-1000.
53. Avanzato, V.A., et al., *Case Study: Prolonged Infectious SARS-CoV-2 Shedding from an Asymptomatic Immunocompromised Individual with Cancer.* Cell, 2020. **183**(7): p. 1901-1912.e9.
54. Schubert, M., S. Lindgreen, and L. Orlando, *AdapterRemoval v2: rapid adapter trimming, identification, and read merging.* BMC Res Notes, 2016. **9**: p. 88.
55. Langmead, B. and S.L. Salzberg, *Fast gapped-read alignment with Bowtie 2.* Nat Methods, 2012. **9**(4): p. 357-9.
56. Li, H., et al., *The Sequence Alignment/Map format and SAMtools.* Bioinformatics, 2009. **25**(16): p. 2078-9.

831 57. McKenna, A., et al., *The Genome Analysis Toolkit: a MapReduce framework for*
832 *analyzing next-generation DNA sequencing data.* Genome Res, 2010. **20**(9): p. 1297-303.

833

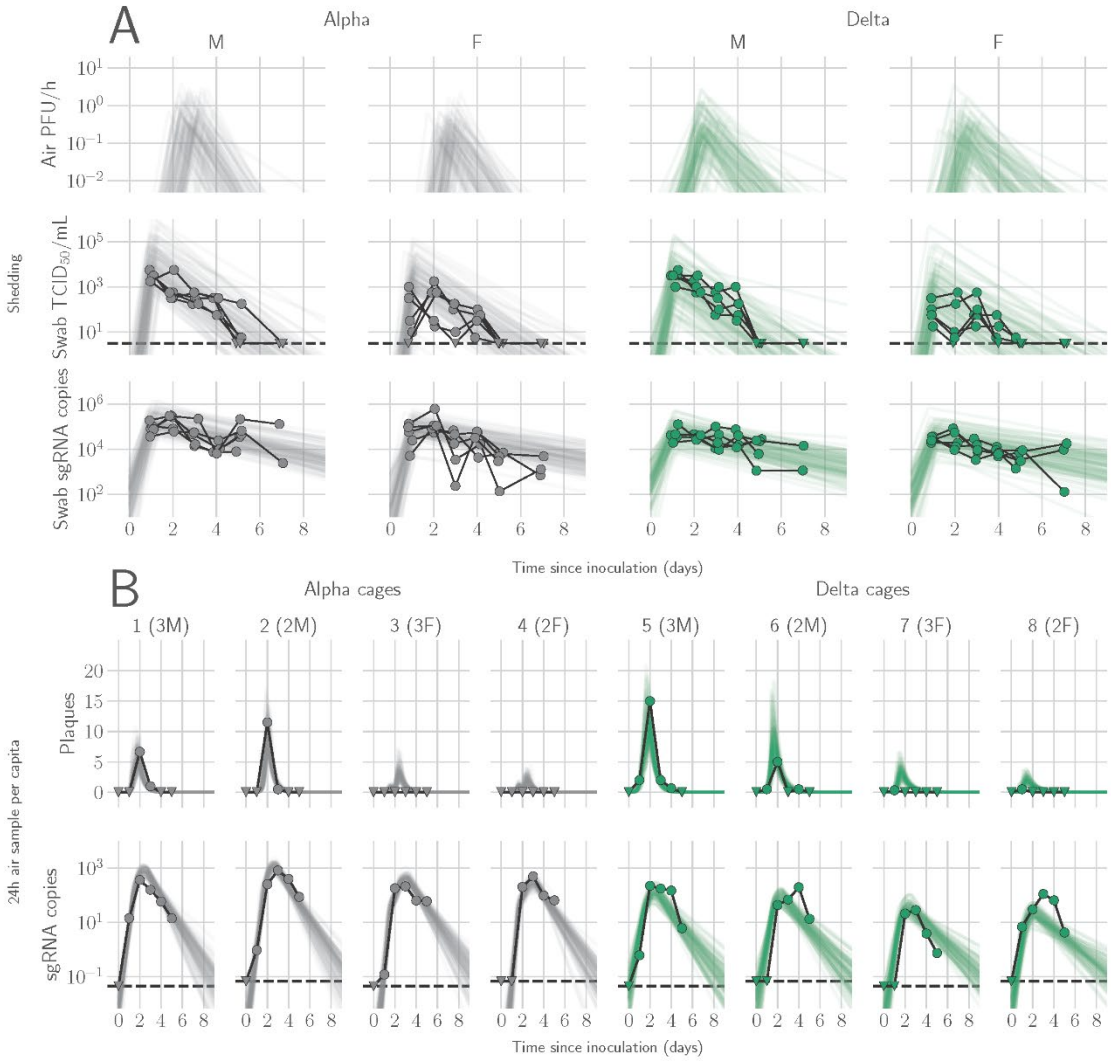

Figure 1. Alpha and Delta variant shedding profiles in oral swabs and air samples. Syrian hamsters were inoculated with 10^3 $TCID_{50}$ via the intranasal route with Alpha or Delta. **A.** Comparison of swab viral load and virus shedding into the air. Inferred profile of air shedding in PFU/h compared to sgRNA levels and infectious virus titers ($TCID_{50}$/mL) in oropharyngeal swabs collected 1, 2, 3, 4, 5, and 7 DPI. Semitransparent lines are 100 random draws from the inferred posterior distribution of hamster within-host kinetics for each of the metrics. Joined points are individual measured timeseries for experimentally infected hamsters; each set of joined points is one individual. Measurements and inferences shown grouped by variant and animal sex. Measurement points are randomly jittered slightly along the x (time) axis to avoid overplotting. **B**. Viral sgRNA and infectious virus (PFU) recovered from cage air sample filters over a 24 h period starting at 0, 1, 2, 3, 4, and 5 DPI. Points are measured values, normalized by the number of hamsters in the cage (2 or 3) to give per-capita values. Downward-pointing arrows represent virus below the limit of detection (0 observed plaques or estimated copy number corresponding to Ct ≥ 40). Semitransparent lines are posterior predictions for the sample that would have been collected if sampling started at that timepoint; these reflect the inferred underlying concentrations of sgRNA and infectious virus in the cage air at each timepoint and are calculated from the inferred infection kinetics for each of the hamsters housed within the cage. 100 random posterior draws shown for each cage. Cages housed 2 or 3 hamsters; all hamsters within a cage were of the same sex and infected with the same variant. Column

852 titles show cage number and variant, with number of and sex of individuals in parentheses. Dotted lines
853 limit of detection. Grey = Alpha, teal = Delta, p-values are indicated where significant. Abbreviations: sg,
854 subgenomic; TCID, Tissue Culture Infectious Dose; PFU, plaque forming unit; F, female; M, male; DPI,
855 days post inoculation.

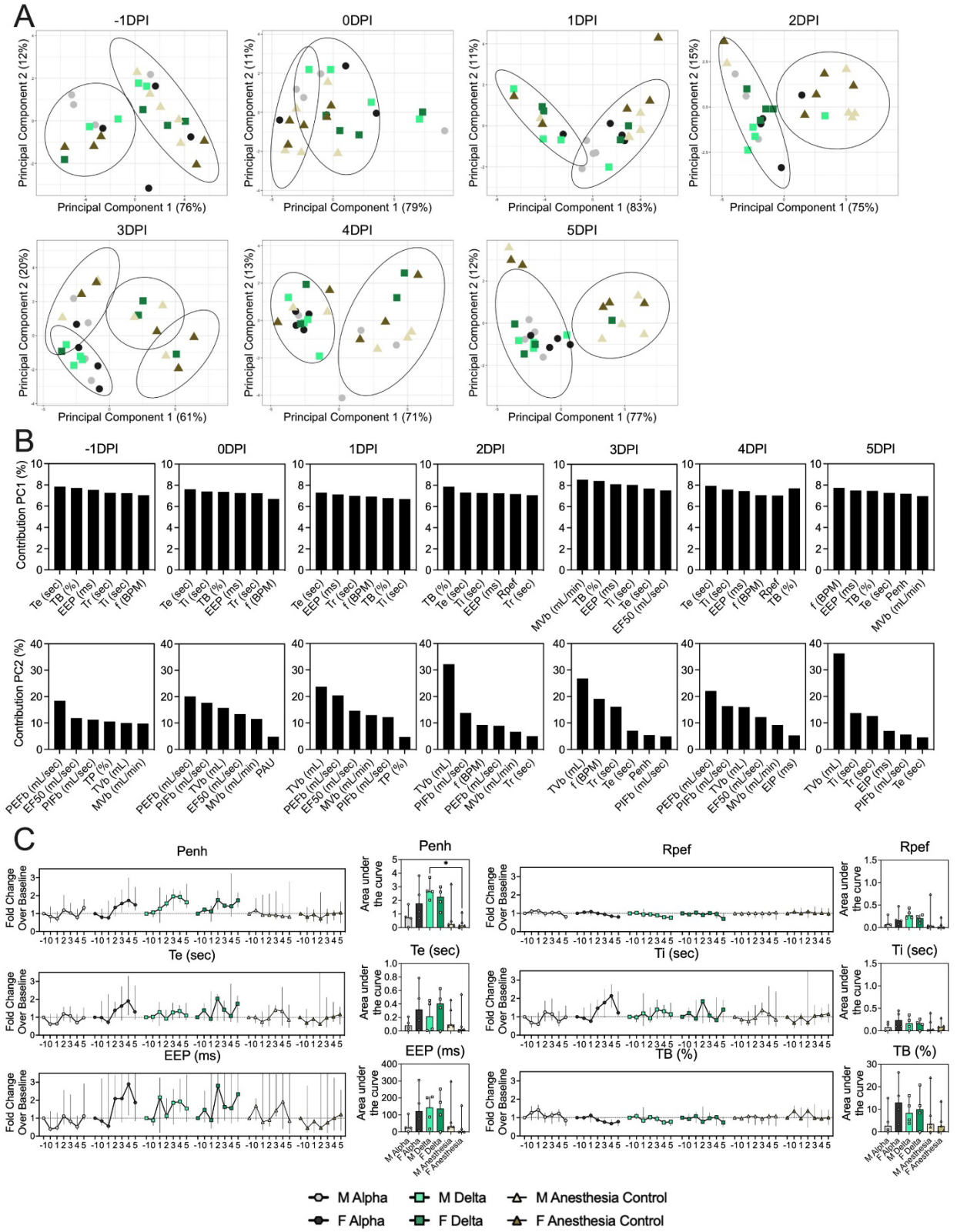
A
-1DPI
0DPI
1DPI
2DPI
3DPI
4DPI
5DPI
Principal Component 1 (76%)
Principal Component 2 (12%)
Principal Component 1 (79%)
Principal Component 2 (11%)
Principal Component 1 (83%)
Principal Component 2 (11%)
Principal Component 1 (75%)
Principal Component 2 (15%)
Principal Component 1 (61%)
Principal Component 2 (20%)
Principal Component 1 (71%)
Principal Component 2 (13%)
Principal Component 1 (77%)
Principal Component 2 (12%)
B
Contribution PC1 (%)
Te (sec)
TB (%)
EEP (ms)
Ti (sec)
f (BPM)
Tr (sec)
Rpef
MVb (mL/min)
EF50 (mL/sec)
Penh
Contribution PC2 (%)
PEFb (mL/sec)
EF50 (mL/sec)
PIFb (mL/sec)
TP (%)
TVb (mL)
MVb (mL/min)
PAU
EIP (ms)
C
Penh
Te (sec)
EEP (ms)
Rpef
Ti (sec)
TB (%)
Fold Change Over Baseline
Area under the curve
M Alpha
F Alpha
M Delta
F Delta
M Anesthesia Control
F Anesthesia Control

856

857 **Figure 2. Lung function and breathing changes after SARS-CoV-2 infection with Alpha and Delta.**
858 Syrian hamsters were inoculated with 10^3 $TCID_{50}$ via the intranasal route with Alpha or Delta. **A.** Lung
859 function was assessed on day -1, 0, 1, 2, 3, 4, and 5 by whole body plethysmography. Principal component
860 analysis was used to investigate individual variance. Depicted are principal component (PC) 1 and 2 for
861 each day, showing individual animals (colors refer to legend on right, sex-separated) and clusters (black
862 ellipses). **B.** Individual loading plots for contributions of top 6 variables to PC1 and 2 at each day. **C.**
863 Relevant subset of lung function parameters. Line graphs depicting median and 95% CI fold change values
864 (left) and area under the curve (AUC, right), Kruskal-Wallis test, p-values indicated where significant. Grey
865 = Alpha, teal = Delta, beige = anesthesia control, light = male, dark = female. Abbreviations: Expiratory time
866 (Te), inspiratory time (Ti), percentage of breath occupied by the transition from inspiration to expiration
867 (TB), end expiratory pause (EEP), breathing frequency (f), peak inspiratory flow (PIFb), peak expiratory
868 flow (PEFb), tidal volume (TVb), minute volume (MVb), enhanced pause (Penh), male (M), female (F).
869

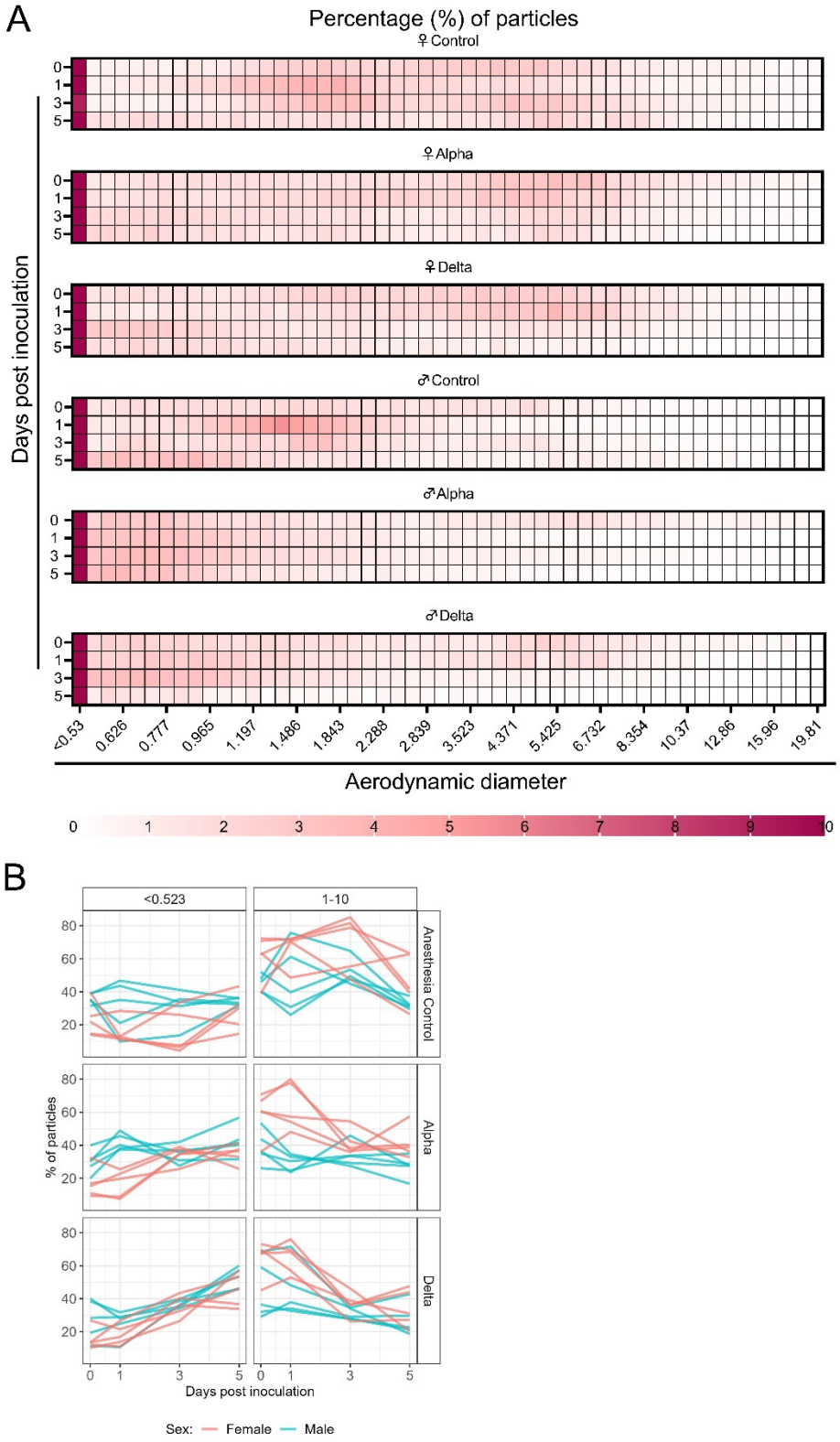
A
Percentage (%) of particles
♀Control
♀Alpha
♀Delta
♂Control
♂Alpha
♂Delta
Days post inoculation
0
1
3
5
<0.53
0.626
0.777
0.965
1.197
1.486
1.843
2.288
2.839
3.523
4.371
5.425
6.732
8.354
10.37
12.86
15.96
19.81
Aerodynamic diameter
0
1
2
3
4
5
6
7
8
9
10
B
<0.523
1-10
Anesthesia Control
Alpha
Delta
% of particles
80
60
40
20
0
1
3
5
Days post inoculation
Sex:
Female
Male

870

871 **Figure 3: Aerodynamic particle analysis of SARS-CoV-2 infected hamsters. A.** Syrian hamsters were
872 inoculated with 10^3 $TCID_{50}$ via the intranasal route with Alpha or Delta. Aerodynamic diameter profile of
873 exhaled particles was analyzed on day 0, 1, 3, and 5. Heatmap shows rounded median percent of total
874 particles across groups, including the anesthesia control group (N = 10, comprising 5 males and 5 females).
875 Colors refer to scale below. **B.** For each animal, line graphs of the percent of particles in the <0.53 and 1-
876 10 μm diameter range by variant group and sex indicated by color. Multiple linear regression performed for
877 each diameter range with group and sex as predictors, F-statistic (3,26) = 9.47 for <0.53 μm model and F-
878 statistic (3,26) = 2.62 for 1-10 μm model, with Tukey multiple comparison adjustment for the three variant-
879 group comparisons (95% family-wise confidence level). For <0.53 range, Male-Female (estimate = -1.7,
880 standard error = 0.888, two-sided p = 0.0659); Alpha-Control (estimate = 2.41, standard error = 1.09, two-
881 sided p = 0.0874), Delta-Control (estimate = 5.40, standard error = 1.09, two-sided p = 0.0001), Delta-Alpha
882 (estimate = 2.99, standard error = 1.09, two-sided p = 0.0280). For 1-10 range, Male-Female (estimate =
883 2.19, standard error = 1.23, two-sided p = 0.0875); Alpha-Control (estimate = -0.633, standard error = 1.51,
884 two-sided p = 0.9079), Delta-Control (estimate = -3.098, standard error = 1.51, two-sided p = 0.1197), Delta-
885 Alpha (estimate = -2.465, standard error = 1.51, two-sided p = 0.2498). Grey = Alpha, teal = Delta, beige =
886 anesthesia control, red = female, blue = male.
887

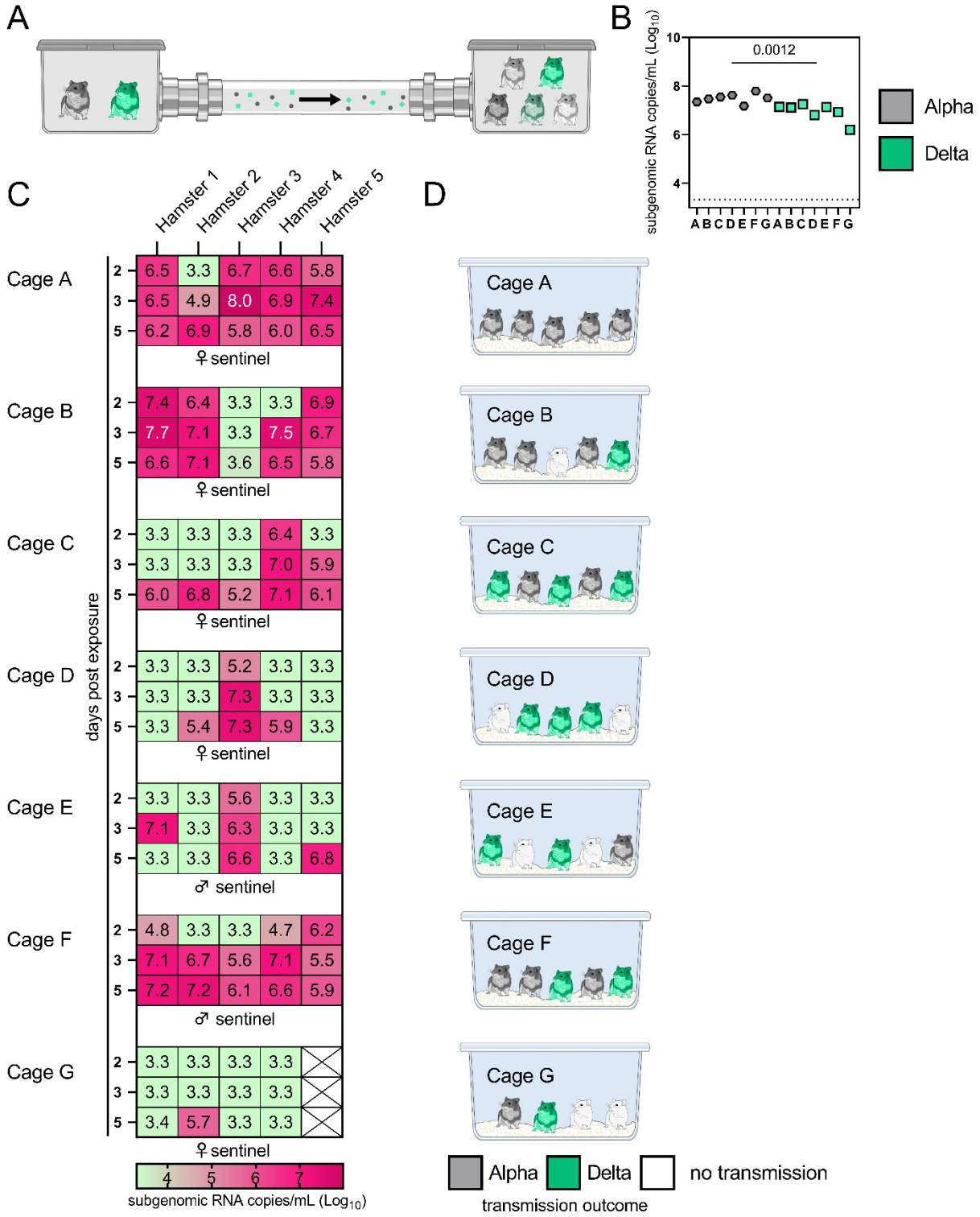

Figure 4. Airborne attack rate of Alpha and Delta SARS-CoV-2 variants. Donor animals (N = 7) were inoculated with either the Alpha or Delta variant with 10^3 $TCID_{50}$ via the intranasal route and paired together

891 randomly (1:1 ratio) in 7 attack rate scenarios (A-G). To each pair of donors, one day after inoculation, 4-5
892 sentinels were exposed for a duration of 4 h (i.e., h 24-28 post inoculation) in an aerosol transmission set-
893 up at 200 cm distance. **A.** Schematic figure of the transmission set-up. **B**. Day 1 sgRNA detected in oral
894 swabs taken from each donor after exposure ended. Individuals are depicted. Wilcoxon test, N = 7. Grey =
895 Alpha, teal = Delta inoculated donors**. C.** Respiratory shedding measured by viral load in oropharyngeal
896 swabs; measured by sgRNA on day 2, 3, and 5 for each sentinel. Animals are grouped by scenario. Colors
897 refer to legend below. 3.3 = limit of detection of RNA (<10 copies/rxn). **D.** Schematic representation of
898 majority variant for each sentinel as assessed by percentage of Alpha and Delta detected in oropharyngeal
899 swabs taken at day 2 and day 5 post exposure by deep sequencing. Grey = Alpha, teal = Delta, white = no
900 transmission.
901

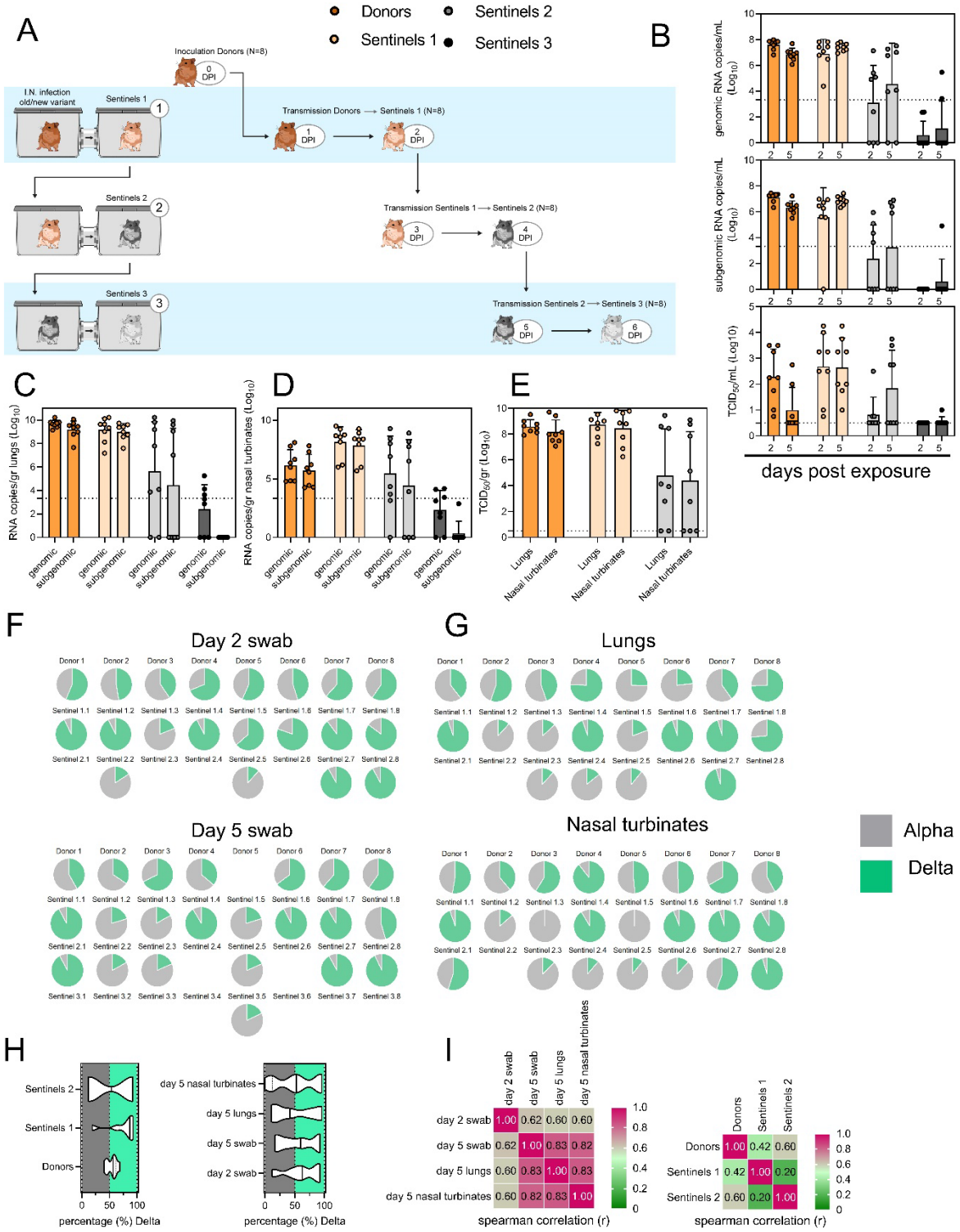

Figure 5. Airborne competitiveness of Alpha and Delta SARS-CoV-2 variants. A. Schematic. Donor animals (N = 8) were inoculated with Alpha and Delta variant with 5 x 10^2 $TCID_{50}$, respectively, via the

905 intranasal route (1:1 ratio), and three groups of sentinels (Sentinels 1, 2, and 3) were exposed subsequently
906 at a 16.5 cm distance. Animals were exposed at a 1:1 ratio; exposure occurred on day 1 (Donors →
907 Sentinels 1) and day 2 (Sentinels → Sentinels). **B.** Respiratory shedding measured by viral load in
908 oropharyngeal swabs; measured by gRNA, sgRNA, and infectious titers on days 2 and day 5 post exposure.
909 Bar-chart depicting median, 96% CI and individuals, N = 8, ordinary two-way ANOVA followed by Šídák's
910 multiple comparisons test. **C/D/E.** Corresponding gRNA, sgRNA, and infectious virus in lungs and nasal
911 turbinates sampled five days post exposure. Bar-chart depicting median, 96% CI and individuals, N = 8,
912 ordinary two-way ANOVA, followed by Šídák's multiple comparisons test. Dark orange = Donors, light
913 orange = Sentinels 1, grey = Sentinels 2, dark grey = Sentinels 3, p-values indicated where significant.
914 Dotted line = limit of detection. **F.** Percentage of Alpha and Delta detected in oropharyngeal swabs taken
915 at days 2 and day 5 post exposure for each individual donor and sentinel, determined by deep sequencing.
916 Pie-charts depict individual animals. Grey = Alpha, teal = Delta. **G.** Lung and nasal turbinate samples
917 collected on day 5 post inoculation/exposure. **H**. Summary of data of variant composition, violin plots
918 depicting median and quantiles for each chain link (left) and for each set of samples collected (right).
919 Shading indicates majority of variant (grey = Alpha, teal = Delta). **I.** Correlation plot depicting spearman r
920 for each chain link (right, day 2 swab) and for each set of samples collected across all animals (left). Colors
921 refer to legend on right. Abbreviations: TCID, Tissue Culture Infectious Dose.